


Article

Preparation and Photothermal Antimicrobial Performance of Triple Linkage Hydrogels

Zekun Chen, Qingyue Yin, Liang Xu, Wenwen Guo and Caihong Tao * 

School of Chemistry and Chemical Engineering, Lanzhou Jiaotong University, Lanzhou 730070, China; 18793178984@163.com (Z.C.)

* Correspondence: taoch@mail.lzjtu.cn; Tel.: +86-931-4956793

Abstract: Often, bacterial infections delay the rate of healing of traumatic wounds, making it critical to improve antimicrobial efficiency. In this paper, titanium nanotubes (TNT) with good antimicrobial and synergistic photothermal properties were used as the core, and mesoporous polydopamine (MPDA) thin films were constructed on their surface. Gold nanoparticles (AuNPs) with excellent photothermal conversion efficiencies (PCE) were incorporated. Finally, a large number of composite nanoparticles were added to polyvinyl alcohol (PVA) and polyethylene glycol (PEG) with wound-restoring ability, and an injectable antimicrobial hydrogel was successfully prepared by a one-pot synthesis. The antimicrobial effect of TNT@MPDA@Au nanoparticles with different concentrations was assessed by in vitro antimicrobial experiments on *Escherichia coli* (*E. coli*) and *Staphylococcus aureus* (*S. aureus*). The higher the concentration of nanoparticles under near-infrared light irradiation (NIR), the stronger the antimicrobial effect. The in vitro cytotoxicity of TNT@MPDA and TNT@MPDA@Au nanoparticles on 293T normal cells was tested through CCK-8 assay. The results show that both nanoparticles have favourable biocompatibility. In this paper, a three-component synergistic photothermal antimicrobial nano-antimicrobial platform was constituted by incorporating MPDA, a photothermal agent with excellent biocompatibility and photothermal properties, and AuNPs with good photothermal properties on TNT with excellent photocatalytic properties.

Keywords: photothermal antibacterial; Au nanoparticles; mechanical property; wound healing



Citation: Chen, Z.; Yin, Q.; Xu, L.; Guo, W.; Tao, C. Preparation and Photothermal Antimicrobial Performance of Triple Linkage Hydrogels. *Coatings* **2024**, *14*, 363. <https://doi.org/10.3390/coatings14030363>

Academic Editors: Daniela Predoi, Carmen Steluta Ciobanu and Alina Mihaela Prodan

Received: 22 January 2024
Revised: 11 March 2024
Accepted: 15 March 2024
Published: 19 March 2024



Copyright: © 2024 by the authors. Licensee MDPI, Basel, Switzerland. This article is an open access article distributed under the terms and conditions of the Creative Commons Attribution (CC BY) license (<https://creativecommons.org/licenses/by/4.0/>).

1. Introduction

The skin, as the biggest tissue of the body, protects against bacteria and viruses, maintains fluid balance and body temperature, and protects internal tissues [1–3]. In the event of a serious injury to the skin (e.g., burns, scalds, cuts, etc.), a wound dressing needs to be applied quickly to the wound to achieve rapid haemostasis, antimicrobial activity, and re-healing of the wound [4,5]. Commonly used haemostatic agents include bandages, fibrin glue, liquids, powders, and hydrogel dressings. Hydrogel dressings can cover the injured area and provide physical assistance for wound restoration [6]. Hydrogels are attracting attention as promising dressings that act as a physical barrier that not only creates a moist environment for skin regeneration but also cools the wound, allowing oxygen to penetrate and promote wound healing [7]. Conventional hydrogels lack injectability, self-healing properties, remodelling, and antimicrobial properties, and have poor mechanical properties, limiting their use and development in the field of wound dressings [8,9]. Thus, there is an urgency to investigate wound dressings that can temporarily replace skin to accelerate wound healing [10].

Polymer blending is one of the most significant current methods in the development of novel polymer materials and is an important means for obtaining materials with a variety of properties [11,12]. As we all know, hydrogel can be divided into natural hydrogel and synthetic hydrogel [13]. Compared with natural hydrogels, synthetic hydrogels are physically cross-linked by hydrogen bonding in a simple and controllable synthesis process, which has the advantages of cheap raw materials, short synthesis time, and easy operation,

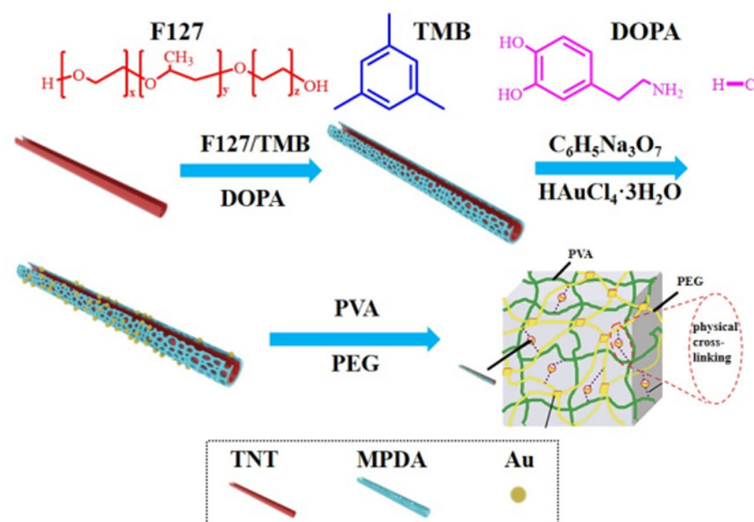
and under certain conditions, synthetic hydrogels can be applied as a liquid or delivered to the body. In addition, they are widely used because of their excellent biocompatibility, biodegradability, ability to carry hydrophilic and hydrophobic nanoparticles, stability, and degradability [14]. At the same time, most synthetic hydrogels are limited in their biological applications due to their low toxicity and the fact that some of the cross-linking agents are not biocompatible. PVA hydrogels are often used as wound dressings due to their biodegradability, non-toxicity, excellent mechanical strength, high elasticity, hydrophilicity, good biocompatibility, and film-forming ability [15]. PEG hydrogels have good biocompatibility, non-toxicity, easy modification, a high drug encapsulation rate, etc., and have a very promising future in hydrogel dressings [16,17].

PEG/PVA hybrid hydrogel dressings are prepared by physical cross-linking, which has the edge of being non-toxic compared to chemical cross-linking [18]. At the present time, the self-healing property of hydrogels is of wide concern in the area of wound dressings. Self-healing hydrogels can automatically repair collapsed networks and maintain their mechanical stability without any external intervention. They can support a moist environment for wounds, absorb exudates, permit oxygen penetration, and can also adapt to changes in the wound [19]. PEG/PVA hybrid hydrogels can provide excellent self-healing properties of the hybrid hydrogel due to the addition of PEG hydrogel, and the dense cross-linked network formed will lock up the water, reduce the evaporation of water, and, meanwhile, improve the mechanical properties [20].

Dopamine has analogous functions to mytilus edulis adhesion proteins, which spontaneously oxidise and polymerise in air under weakly alkaline conditions to form polydopamine (PDA), which can adhere to the surface of almost all types of materials [21,22]. PDA is a polymer with abundant functional groups, excellent hydrophilicity and biocompatibility, and it also has many applications such as drug loading and precious metal nanoparticle loading [23]. Photothermal therapy (PTT) is widely used in the antimicrobial field due to its advantages of being non-invasive, having a short treatment time, and being a relatively safe technique [24]. PTT is based on the conversion of light energy (usually in the near-infrared (NIR) region) into thermal energy to induce subsequent cellular necrosis or apoptosis [25]. AuNPs have been frequently used as a photothermal prophylactic agent due to their unique optical properties and ability to be readily adsorbed [26]. The photon energy is efficiently and rapidly converted into thermal energy by direct excitation of surface plasmon resonance (SPR) in AgNPs [27]. Therefore, the incorporation of noble metal gold nanoparticles can significantly improve the photothermal conversion rate. AuNPs are often used as photothermophiles because of their unique optical properties and their ability to adsorb easily [28]. And the addition of precious metal gold nanoparticles can significantly enhance the photothermal conversion rate. For example, Liu et al. coated PDA with gold nanobrick pyramids (AuNBPs), and it can be clearly measured that the photothermal conversion rate is higher than that of AuNBPs alone [29]. And Wang et al. also believed that PDA-coated AuNPs exhibit enhanced photothermal properties by taking advantage of the strong light absorption and photothermal effects of PDA [30]. Titanium dioxide (TiO_2) is one of the most promising photocatalysts for many fields because of its relatively low cost, low toxicity, high stability, and high efficiency [31,32]. Titanium nanotubes (TNTs) exhibit good photocatalytic performance during the oxidation process [33]. The photocatalytic performance of TNTs mainly originates from their own special electronic structure and good photovoltaic properties. The results showed that hydroxyl ions (OH^-), H_2O_2 , and oxidising oxygen radicals enhanced the activity of TNTs [34,35]. And the noble metal nanoparticles (AuNPs) can be used as co-catalysts, which can not only enhance the photothermal conversion rate of the materials but also promote the separation of an electron-hole ($e\text{-H}^+$) and facilitate the interfacial electron transfer, which improves the surface reaction activity [36].

In this study, TNT@MPDA@Au@PVA/PEG hydrogels with photocatalytic and photothermal antibacterial properties were prepared. The anatase TNTs were prepared by the hydrothermal method, and the mesoporous polydopamine (MPDA) was constructed on the superficies of TNTs by a layer-by-layer self-assembly process to form a TNT@MPDA core-shell

structure. Then, AuNPs were deposited in situ on the surface and in the pores of TNTs and MPDA. Finally, the above composite nanotubes were mixed with pure PVA/PEG hydrogel to prepare the desired injectable antimicrobial hydrogels. The surface morphology and microsphere size were analysed using scanning electron microscopy (SEM). The functional groups of the prepared materials were proved by infrared visible spectroscopy (FTIR). The pore size and pore volume of the nanotubes were determined by nitrogen adsorption and desorption experiments. A cytotoxicity assay tested the cell survival of the nanotubes against normal cells. In addition, the antimicrobial properties of the injectable photothermal antimicrobial hydrogels were investigated against *S. aureus* and *E. coli* before and after light exposure, as well as the mechanical properties of the hydrogels in practical applications (Scheme 1).



Scheme 1. Experimental section.

2. Materials

Titanium oxide (TiO₂, AR, 99.5%), 1, 3, 5-Trimethylbenzene (TMB, AR, 97%), Tris (hydroxymethyl) aminomethane (Tris, 99.9%), Dopamine hydrochloride (DOPA, 98%, AR), Sodium chloride (NaCl, AR, 99%), Tryptone (RG), and NaOH (AR, 99.5%) were purchased from Aladdin industrial Inc. Pluronic[®] F-127 (Ontario, CA, USA) was obtained from Sigma-Aldrich (St. Louis, MO, USA). Agar powder (BR) and Poly(ethylene glycol) (4000 Mw) were purchased from Macklin (Shanghai, China). Gold (III) chloride trihydrate (HAuCl₄·3H₂O, AR, 99%) and Yeast extract were obtained from Solelybio mall (Shanghai, China). Ethanol (AR, 99.7%), Acetone (AR, 95%), Trisodium citrate dehydrate (AR, 99%) and PVA polymer (44.05 Mw, degree of hydrolysis 98%–99%) were purchased from Sinopharm Group Chemical Reagent Co., Ltd. (Shanghai, China) (Table 1).

Table 1. Instruments used in the experiment.

Instrument Model	Model Number	Manufacturer (of a Product)
High-resolution transmission electron microscopy (TEM)	FEI Corp TF 20	Japan JEOL Corporation, Tokyo, Japan
High-speed freezing centrifuge	GL-G20-II	Shanghai Anting Instrument Co., Shanghai, China
Ultraviolet spectrophotometer (UV-Vis)	NanoDrop 2000c	Tianmei Instrument Co., Shanghai, China
X-ray photoelectron spectroscopy (XPS)	pHI-5702	Physical Electronics Corporation, Chanhassen, MN, USA
Zeta potential and particle size analyser	90plus Pals	Brookhaven Corporation, Lexington, MA, USA
Field emission scanning electron microscope (FESEM)	JSM-6701F	Japan JEOL Corporation, Tokyo, Japan
X-ray diffractometer (XRD)	XRD7000, 40 kV/150 mA	Shimadzu Corporation, Kyoto, Japan
Fourier transform infrared spectrometer (FTIR)	BrukerIFS66V/S Fourier	Bruker Corporation, Ettlingen, Germany
Rotary Bath Oscillator	SHZ-82	Jiangsu Zhengji Instrument Co., Changzhou, China
Magnetic stirrer	85-1	Shanghai Silo Instrument Co., Shanghai, China
Analytical balance	FA2004	Shanghai Liangping Instrumentation Co., Shanghai, China

2.1. Synthesis of TNT Nanoparticles

A total of 2.5 g of TiO_2 was mixed with 35 mL of a 10 M sodium hydroxide (NaOH) solution in a 50 mL autoclave. The autoclave was sealed and the reaction was conducted at 140 °C for 48 h. After the reaction, a white gel was obtained [37]. The gel was neutralized by adding distilled water. Then, it was immersed in 10 mL of a 0.1 M hydrochloric acid (HCl) solution for 1 h [38]. The soaked gel was dried at 105 °C for 5 h to obtain the TNTs [39].

2.2. Synthesis of TNT@MPDA Nanoparticles

The above-mentioned 60 mg of TNTs were dispersed in 2 mL of water using ultrasonic waves. A total of 65 mL of H_2O and 60 mL of EtOH were measured, and 0.36 g of F127 and 625 μL TMB were added to the mixture of ethanol and water almost simultaneously. The mixture was then stirred magnetically for a duration of 30 min. Furthermore, 90 mg of Tris was dissolved in 5 mL of water and subsequently added to the mixture. After stirring for a period of 2 min, 60 mg of DOPA and the previously dispersed TNT were added swiftly. The mixture was then stirred at a temperature of 40 °C for 24 h. The resulting nanoparticles were washed and placed in a desiccator at 50 °C for 6 h in order to obtain TNT@MPDA nanotubes [40,41].

2.3. Synthesis of TNT@MPDA@Au Nanoparticles

A total of 1.01 g of trisodium citrate was dissolved in 18 mL of distilled water. Next, 60 mg TNT@MPDA nanotubes were dispersed in 2 mL of water and added to the trisodium citrate solution. Finally, 2 mg of $\text{HAuCl}_4 \cdot 3\text{H}_2\text{O}$ was added to the mixture. The mixture was stirred at room temperature for 2 h. Then, it was centrifuged and washed three times with water to obtain TNT@MPDA@Au nanotubes [28].

2.4. Synthesis of TNT@MPDA@Au@PVA/PEG Composite Hydrogel

A total of 15 g of PVA was gradually added to 200 mL of distilled water and the resulting mixture was magnetically stirred at a temperature of 95 °C until a uniform and transparent solution was achieved. TNT@MPDA@Au nanotubes were incorporated into the PVA solution and subjected to stirring for 4 h [42,43]. Subsequently, 5 g of PEG was introduced into the solution, and the stirring process was sustained for 0.5 h. The obtained solution was transferred into a plastic mould, frozen at -20 °C for 8 h, subsequently thawed at room temperature for 4 h, and subjected to 3 cycles of freezing and thawing to yield composite hydrogels consisting of TNT@MPDA@Au@PVA/PEG [44].

2.5. Photothermal Performance Test

A total of 1 mL of TNT@MPDA@Au nanotube suspension at concentrations of 2 mg/mL, 4 mg/mL, 6 mg/mL, and 8 mg/mL was dispersed in a Xilin flask. The suspension was horizontally illuminated using a NIR laser (808 nm, $2 \text{ W}/\text{cm}^{-2}$) at a distance of 2 cm (the temperature was recorded every minute for a total of 10 min using an electronic thermometer). This process of irradiation and temperature measurement was conducted to investigate the photothermal stability of TNT@MPDA@Au nanotubes [45].

A total of 1 mL of TNT@MPDA@Au nanotubes at a concentration of 2 mg/mL was selected and irradiated vertically with a near-infrared laser. The temperature was recorded every minute using an electronic thermometer for a total of 10 min. The cycle curves for temperature rise and temperature fall were determined in this experiment [46].

In order to investigate the synergistic photothermal effect of TNT@MPDA@Au nanotubes, the photothermal conversion efficiency of the composite nanotubes was investigated using a near-infrared laser with deionized water as a blank control. The photothermal conversion efficiency of the TNT@MPDA@Au nanotubes was calculated using Formulas (1)–(3) [47,48]:

$$\eta = \frac{hS(T_{\max, m} - T_s)}{I(1 - 10^{-A_\lambda})} \quad (1)$$

$$\tau_s = \frac{m_s C_s}{hS} \quad (2)$$

$$t = -\tau_s \ln(\Delta T / \Delta T_{\max}) \quad (3)$$

h —heat transfer coefficient;

A_{808} —absorbance of the sample at 808 nm;

S —specific surface area of the container;

I —laser power (2 W);

m_s —the quality of the water;

C_s —heat capacity of water (4.2 J/g °C);

ΔT —difference between the temperature at time t and the ambient temperature;

ΔT_{\max} —difference between maximum temperature and ambient temperature.

2.6. In Vitro Cytotoxicity Test

The cytotoxicity of TNT@MPDA nanotubes and TNT@MPDA@Au nanotubes was assessed using the Cell Counting Kit-8 (CCK-8). 293T cells were seeded in 96-well plates at a density of 7000 cells/well, using high-glucose DMEM medium supplemented with 10% fetal bovine serum. The plates were incubated at 37 °C in a cell incubator with a gas mixture of 95% air and 5% CO₂ for 24 h. Following this, the original medium was replaced with 100 µL of fresh DMEM medium containing 10% fetal bovine serum. Four groups of particles (Group 1: TNT@MPDA, Group 2: TNT@MPDA + NIR, Group 3: TNT@MPDA@Au, Group 4: TNT@MPDA@Au + NIR) were diluted to different concentrations and added to the 96-well plates [49]. The plates were then returned to the cell incubator for an additional 24 h incubation period. Subsequently, the drug-containing medium was discarded from each well, and the cells were washed three times with PBS solution. A total of 10 µL of CCK-8 solution was added to each well, and the plates were placed back in the cell incubator for 1.5 h. The optical density (OD) value of each well was measured at a wavelength of 450 nm using a microplate reader [50]. Cell viability was calculated using the following Formula (4):

$$\text{OD} = [(A_s - A_b) / (A_c - A_b)] \times 100\% \quad (4)$$

A_s was the experimental group, A_c was the negative control group, A_b was the blank control group.

2.7. Bacteriostasis Experiments

LB liquid medium was prepared by adding 10 g of NaCl, 10 g of tryptone, 5 g of yeast extract, and 1 L of H₂O. A total of 100 mL of the above solution was added to each of the 4 conical flasks and stored in a sealed container for later use. Then, 16 g of agar powder was added to the remaining 600 mL of the above solution, and the mixture was equally divided and added to 4 conical flasks, sealed and set aside. All instruments were sterilized, and 15–20 mL of culture solution was added to each Petri dish, which was placed flat on the surface and left to cool. A bacterial suspension was formed by scraping off *E. coli* and *S. aureus* from rings and adding them to 100 mL of LB medium [51].

The 2 groups of bacterial suspensions were stirred at 37 °C for 16 h and then diluted to a concentration of 1×10^8 CFU/mL. After that, 30 µL of both sets of bacterial suspensions were added to the solidified agar Petri dishes, and the suspensions were well scraped on the dishes using a triangular applicator stick. The suspensions of TNT@MPDA@AuNPs with concentrations of 20 mg/mL, 40 mg/mL, and 80 mg/mL were slowly added dropwise to the filter paper. Finally, the Petri dishes were incubated in an incubator at 37 °C for 12 h to determine their antibacterial properties. After 24 h, the suppression ring was irradiated for 10 min using a near-infrared laser [50].

2.8. Swelling and Degradation Behaviour of Hydrogels

The freeze-dried hydrogel was immersed in phosphate-buffered saline (PBS) solution with a pH of 7.4 and a temperature of 37 °C. The hydrogel was removed at various time

intervals to measure its weight when wet. The swelling ratio (S) of the hydrogels was calculated using Equation (5):

$$S = (W_t - W_0)/W_0 \times 100\% \quad (5)$$

where W_t denotes the weight of the hydrogel at moment t , and W_0 is the initial weight of the freeze-dried hydrogel [6].

The degradation behaviour of the hydrogels was investigated in PBS at a temperature of 37 °C and a pH of 7.4. The hydrogel was taken out at different time points to determine its weight after being freeze-dried. The residual weight (R) was calculated using Formula (6):

$$R = W_i/W_f \times 100\% \quad (6)$$

where W_i is the dry weight of the hydrogel at moment i , and W_f is the initial weight of the freeze-dried hydrogel [42].

2.9. Mechanical Properties of Hydrogels

The mechanical properties of all cuboid hydrogel samples (length: 15 mm, width: 10 mm, height: 1.5 mm) were analysed using Stable Micro Systems, a company based in the Godalming, UK. The compressive properties of hydrogels were tested at a constant compression rate of 10 mm/s⁻¹. The tensile properties of the rectangular hydrogels were studied at a tensile rate of 0.1 mm/s⁻¹ at room temperature and the stress-strain curves were recorded [8].

3. Results and Discussion

3.1. Morphology and Composition Characterization of TiO₂TNTs@MPDA@Au Nanotubes Antibacterial Material

PDA was coated on the surface of TNT as a core by utilizing the self-polymerization of DOPA in a weakly alkaline solution. The template agent was then removed by extraction to obtain TNT@MPDA nanotubes with mesoporous structure. Finally, AuNPs were deposited in situ on the surface and in the pores of MPDA and TNT. Figure 1a shows that the average pipe length and diameter of the TNTs were around 215 nm and 10 nm. The inset in the upper-right of Figure 1a showed that the TNTs belonged to a typical polycrystalline structure. As could be observed in Figure 1b, the clear core-shell structure with a tube diameter up to about 30 nm and a significantly roughened surface indicated that MPDA was successfully encapsulated on the TNT surface [38].

In Figure 1c it can be clearly observed that AuNPs were heavily loaded on the MPDA surface and mesopores, and a small amount was present in the pores and surface of the TNTs. The first inset in the top-right of Figure 1c shows that AuNPs belonged to a typical polycrystalline structure. The second inset shows that the lattices of the AuNPs were 0.2 nm, and the third inset shows that the average size of the AuNPs was about 6.5 nm. Due to the presence of mesoporous in MPDA, a larger loading of small-sized Au NPs could be enabled. Combined with the FESEM image of TNT@MPDA@Au nanotubes (Figure 1e), it was clear that the AuNPs were well distributed on the nanotube surface. Figure 1d shows the FESEM of the TNTs, and the crisscrossed and smooth-surfaced tubes can be distinctly observed, which further estimates the successful preparation of TNTs. In Figure 1e, which is the FESEM of TNT@MPDA@Au nanotubes, it can be seen that the tube diameter of the nanotubes was obviously coarser than that of Figure 1d, and the small-size AuNPs with very small particle sizes were uniformly distributed on the surface. As shown in Figure 1f, elemental analysis was used to determine the composition of Au, N, O, Ti, and C in the nanosystems, indicating the successful preparation of TNT@MPDA@Au nanotubes.

The surface chemical element composition of TNT@MPDA nanotubes and TNT@MPDA@Au nanotubes was investigated by XPS. As shown in Figure 2i, the wide-scan XPS spectra of TNT@MPDA nanotubes showed strong peaks of C1s, and O1s and weak peaks of N1s and Ti2p. The C1s, N1s, O1s, and Ti2p peaks were fitted, respectively (Figure 2a,c,e,g). As shown in Figure 2a, the C1s splitting peaks in TNT@MPDA nanotubes were fitted

into 3 peaks, of which 284.23 eV were attributed to C–C in MPDA, and 285.21 eV and 286.18 eV were attributed to C–N and C–O in MPDA, respectively. As shown in Figure 2c, the N1s splitting of TNT@MPDA nanotubes fitted two peaks, and the peaks at 398.18 eV and 399.83 eV corresponded to N atoms in C=N–R and R–NH₂, respectively, which is consistent with the chemical environment of N elements in DOPA molecules [52]. As shown in Figure 2e, the O1s splitting peaks were fitted as 3 peaks at 530.03 eV, 531.84 eV, and 532.68 eV, which were, respectively, consistent with the O atomic peaks of –OH, C–O, and C=O in MPDA [53]. Thus, the successful preparation of MPDA could also be demonstrated laterally. The appearance of the C=O peak was attributed to the oxidized catechol groups in the DOPA structure to form quinone. As shown in Figure 2g, the Ti2p splitting peaks were fitted as 3 peaks at 458.78 eV, 458.21 eV, and 463.91 eV; 458.78 eV and 458.21 eV belonged to Ti2p_{3/2} and 463.91 eV belonged to Ti2p_{1/2}. The appearance of Ti2p peaks further indicated the successful preparation of TNTs.

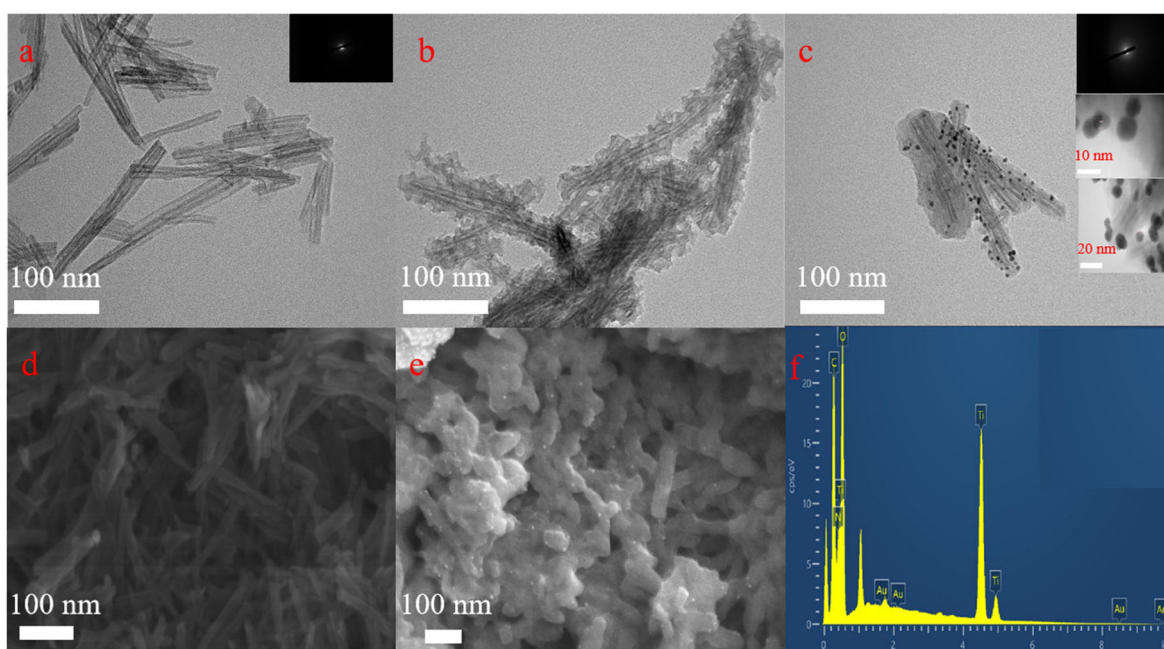


Figure 1. TEM images of (a) TNTs, (b) TNT@MPDA, and (c) TNT@MPDA@Au nanotubes, FESEM images of (d) the TNTs and (e) the TNT@MPDA@Au nanotubes. EDS images of (f) TNT@MPDA@Au nanotubes.

As shown in Figure 2j, the wide-scan XPS spectra of TNT@MPDA@Au nanotubes showed strong peaks of C1s and O1s, and weak peaks of N1s, Ti2p, and Au4f. The Au4f, C1s, O1s, and Ti2p peaks (Figure 2b,d,f,h) were fitted, respectively. The subpeak fitting of Au4f in the total spectrum of Figure 2b showed that the 2 peaks at 83.42 eV and 83.87 eV belonged to Au4f_{7/2} and the 2 peaks at 87 eV and 87.46 eV belonged to Au4f_{5/2}, further confirming the successful preparation and the attachment of AuNPs [36].

As shown in Figure 3a, Curves A and B, respectively, represent the FTIR of TNTs and TNT@MPDA@Au nanotubes. In the FTIR, a broad peak appeared at 490 cm^{−1} belonging to the Ti–O bond, which further proved the successful preparation of TNTs. The peaks at 1380 cm^{−1}, 1620 cm^{−1}, and 3180 cm^{−1} represented the C–H bending vibration within the benzene ring, the backbone vibration of the benzene ring, and the C=C stretching vibration within the benzene ring, respectively. It indicated that MPDA was successfully prepared on TNT [46,54]. As shown in Figure 3b, the peak at 537 nm is the characteristic peak position of Au NPs, which also indicates the successful modification of AuNPs particles. At 808 nm, there is a significant enhancement of photothermal performance with TNT@MPDA loaded with AuNPs, which suggests that the 3-component photothermolysis agent of TNTs, MPDA, and AuNPs has the effect of enhancing photothermal therapy.

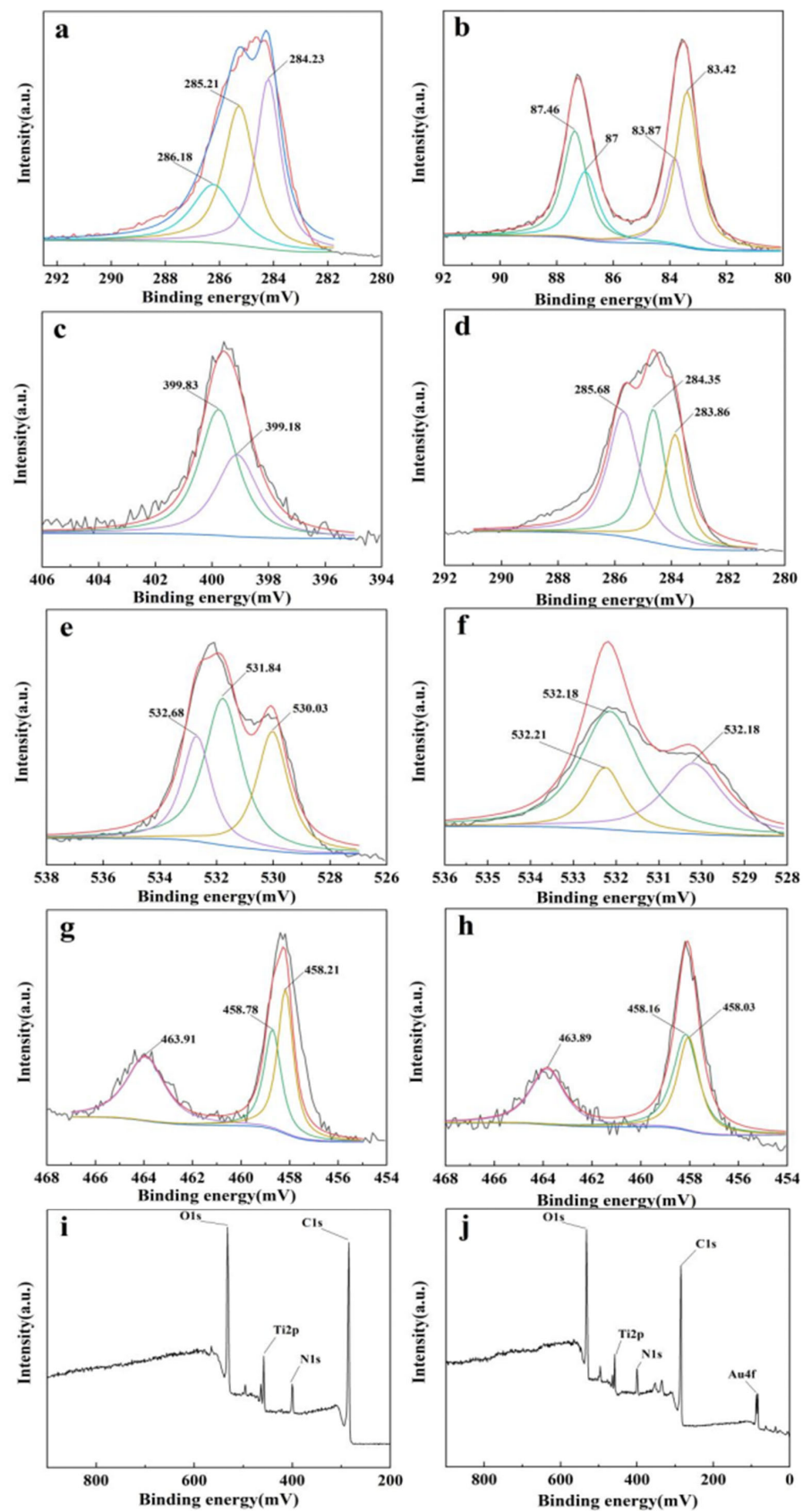


Figure 2. The high-definition XPS of (a) C1s, (c) N1s, (e) O1s, (g) Ti2p, and (i) XPS full spectrum of TNT@MPDA nanotubes. The high-definition XPS of (b) Au4f, (d) C1s, (f) O1s, (h) Ti2p, and (j) XPS full spectrum of TNT@MPDA@Au nanotubes.

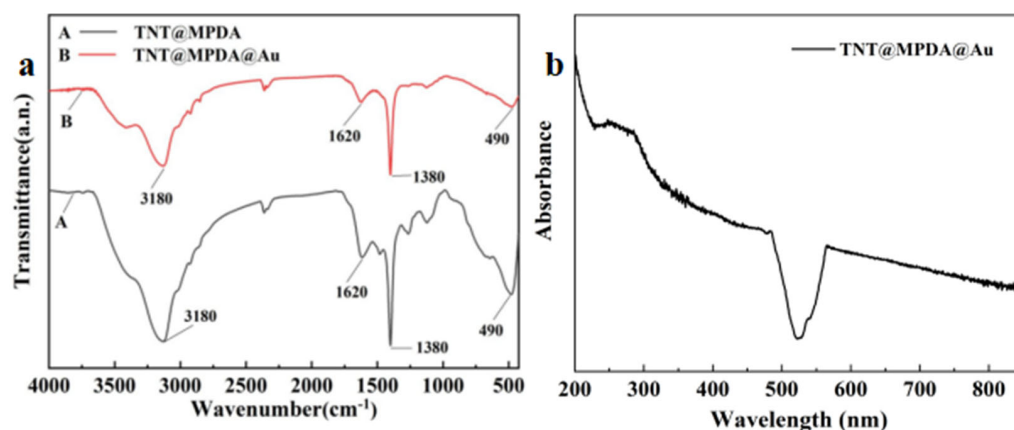


Figure 3. (a) FTIR spectra of TNT@MPDA nanotubes and TNT@MPDA@Au nanotubes. (b) UV-Vis absorption spectrum of TNT@MPDA@Au nanotubes.

The XRD spectra of anatase TiO_2 nanopowders and TNTs of anatase are shown in Figure 4a. The corresponding peaks of TNTs at 2θ values were 25.3° , 37.8° , 48.0° , 53.9° , 55.1° , 62.7° , and 68.8° , which correspond to the (101), (004), (200), (105), (211), (204), and (116) planes, respectively. Using the JCPDS 21-1272 card, these values are attributed to the anatase phase of TNTs [31,55]. The peak at 27.4° in the anatase TiO_2 nanopowders indicated the presence of rutile TiO_2 , whereas there was no diffraction peak for the rutile phase in TNTs. This might be due to the transformation from rutile to anatase during the hydrothermal process [38]. As shown in Figure 4b, diffraction peaks corresponding to monoclinic Au phases at $\theta = 44.4^\circ$, 64.5° , and 77.5° , corresponding to the (220), (322), and (431) planes identified after the attachment of AuNPs [36].

As shown in Figure 4c, the stability of TNT@MPDA nanotubes and TNT@MPDA@Au nanotubes was investigated by Zeta potential measurements. The larger the absolute value (positive and negative) of the Zeta potential, the better the stability. The Zeta potential of TNT@MPDA nanotubes was -67.23 mV (between 60 and 80 mV), indicating that the synthesized TNT@MPDA nanotubes had terrific stability. The Zeta potential of TNT@MPDA@Au nanotubes was -57.93 mV (between 40 and 60 mV), indicating that the synthesized TNT@MPDA@Au nanotubes had good stability. The Zeta potential value decreases because the reduction in Au^+ ions to metallic Au consumes a certain amount of negatively charged MPDA groups; however, the nanosystem still has good stability in an aqueous solution.

Usually, the dimensions measured by DLS tend to be much larger than those measured by TEM. As shown in Figure 4d, the tube length of TNT@MPDA nanotubes had a hydrated particle size of about 615 ± 0.1 nm, and the tube diameter of TNT@MPDA@Au nanotubes had a hydrated particle size of about 37 ± 0.1 nm. The DLS-measured tube lengths of TNT@MPDA and the tube diameters of TNT@MPDA@Au nanotubes were compared to those measured by TEM and are significantly larger.

The mesoporous structure of TNT@MPDA@Au composite nanotubes was investigated using N_2 adsorption–desorption, as shown in Figure 4e,f. As shown in Figure 4e, the TNT@MPDA@Au composite nanotubes conformed to the II isothermal adsorption curve, indicating that the material was a mesoporous adsorbent material [49]. As shown in Figure 4f, the specific surface area of the TNT@MPDA@Au composite nanotubes was $147.59 \text{ m}^2\text{g}^{-1}$, the pore volume was $0.409 \text{ cm}^3\text{g}^{-1}$, and the pore diameter was 12.16 nm.

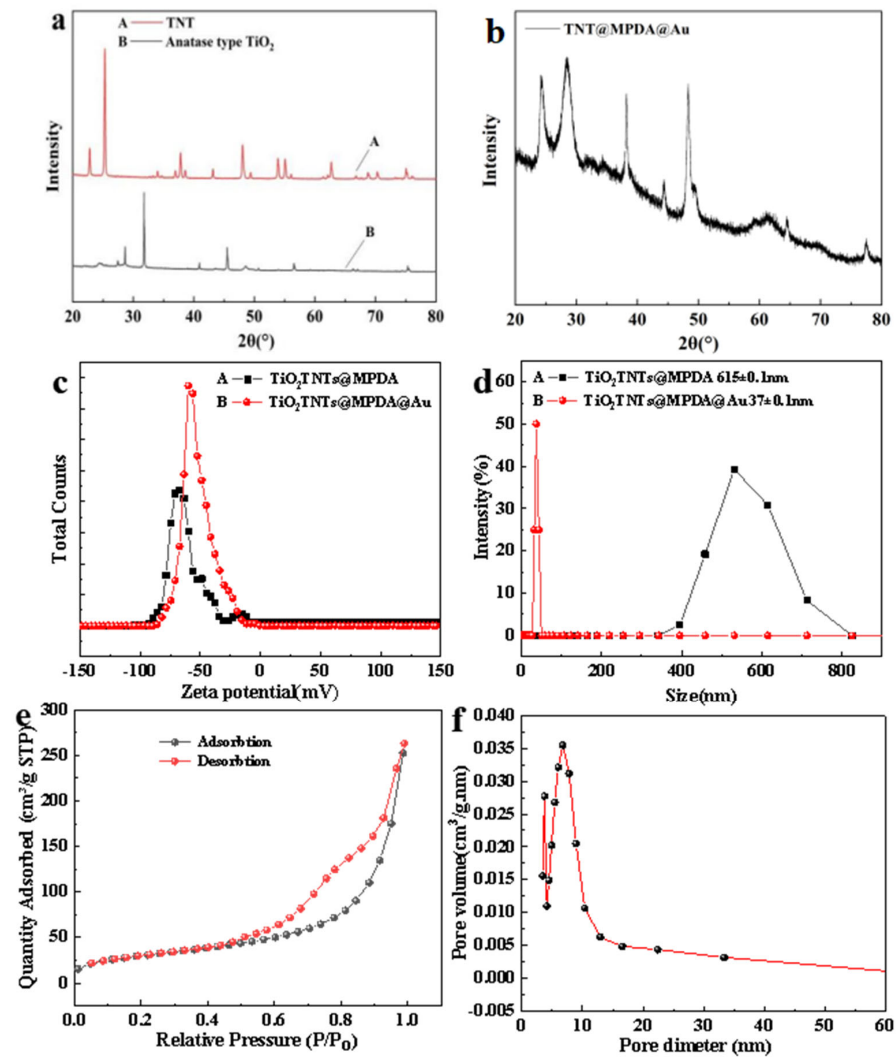


Figure 4. (a) XRD spectrum of anatase TiO_2 nanopowders and the produced titanate nanotube. (b) XRD spectrum of TNT@MPDA@Au nanotubes. (c) Zeta potential curves and (d) hydration kinetic particle size of the TNT@MPDA nanotubes and the TNT@MPDA@Au nanotubes. (e) N_2 adsorption-desorption curves and (f) pore size distribution plots of the TNT@MPDA nanoparticles.

3.2. Photothermal Performance

The photothermal conversion properties of the prepared TNT@MPDA@Au nanotubes were measured under different conditions. Figure 5a shows the curves of temperature variation with time and concentration of TNT@MPDA@Au nanotubes irradiated for 10 min at concentrations of (2 mg/mL, 4 mg/mL, 6 mg/mL and 8 mg/mL), respectively. The results show that within 10 min of irradiation time, the longer the irradiation time and the greater the TNT@MPDA@Au nanotube concentration, the greater the temperature rise. The maximum temperature reached 57.7 °C at a concentration of 8 mg/mL. The maximum temperature difference of TNT@MPDA@Au nanotubes at different concentrations, shown in Figure 5b, was 30.5 °C (8 mg/mL), which was slightly higher compared to the remaining 3 concentration gradients, indicating that the nanotubes had good photothermal properties. The absorbance of TNT@MPDA@Au nanotubes at 808 nm was measured by UV-Vis as 0.246. Figure 5c shows the temperature rise of 2 mg/mL TNT@MPDA@Au nanotubes within 10 min of exposure to near-infrared light and the natural temperature drop after 10 min of stop exposure. According to Formulas (1)–(3), the photothermal efficiency of the TNT@MPDA@Au nanotubes could be calculated as 51.2%, indicating that the TNT@MPDA@Au nanotubes had high photothermal conversion performance [28].

Then, the photothermal stability of the material was tested. Figure 5d showed that the temperature of TNT@MPDA@Au nanotubes had no obvious change after four cycles of near-infrared light irradiation, indicating that TNT@MPDA@Au nanotubes had good photothermal stability. As shown in Figure 5e, it can be clearly seen that TNT@MPDA has a more long-lasting, superior photothermal performance than TNT@Au. However, in the first two minutes, TNT@Au showed better photothermal performance, which might be attributed to the sensitivity and rapidity of Au NPs under photothermal stimuli. Similarly, the same properties of Au NPs are exhibited in this curve for TNT@MPDA@Au. More interestingly, the maximum temperature of TNT@Au is only 4.6 °C higher relative to the maximum temperature of TNT. However, the maximum temperature of TNT@MPDA@Au is surprisingly 5.8 °C higher relative to that of TNT@MPDA. This result further demonstrates that our prepared TNT@MPDA@Au has good mutual synergy to promote photothermal sterilisation. Figure 5f shows the relationship between cooling time and temperature driving force of TNT@MPDA@Au nanotubes. The thermal equilibrium constant $\tau_s = 452.20$ was tested for TNT@MPDA@Au solution at a temperature of 2 mg/mL during the cooling process.

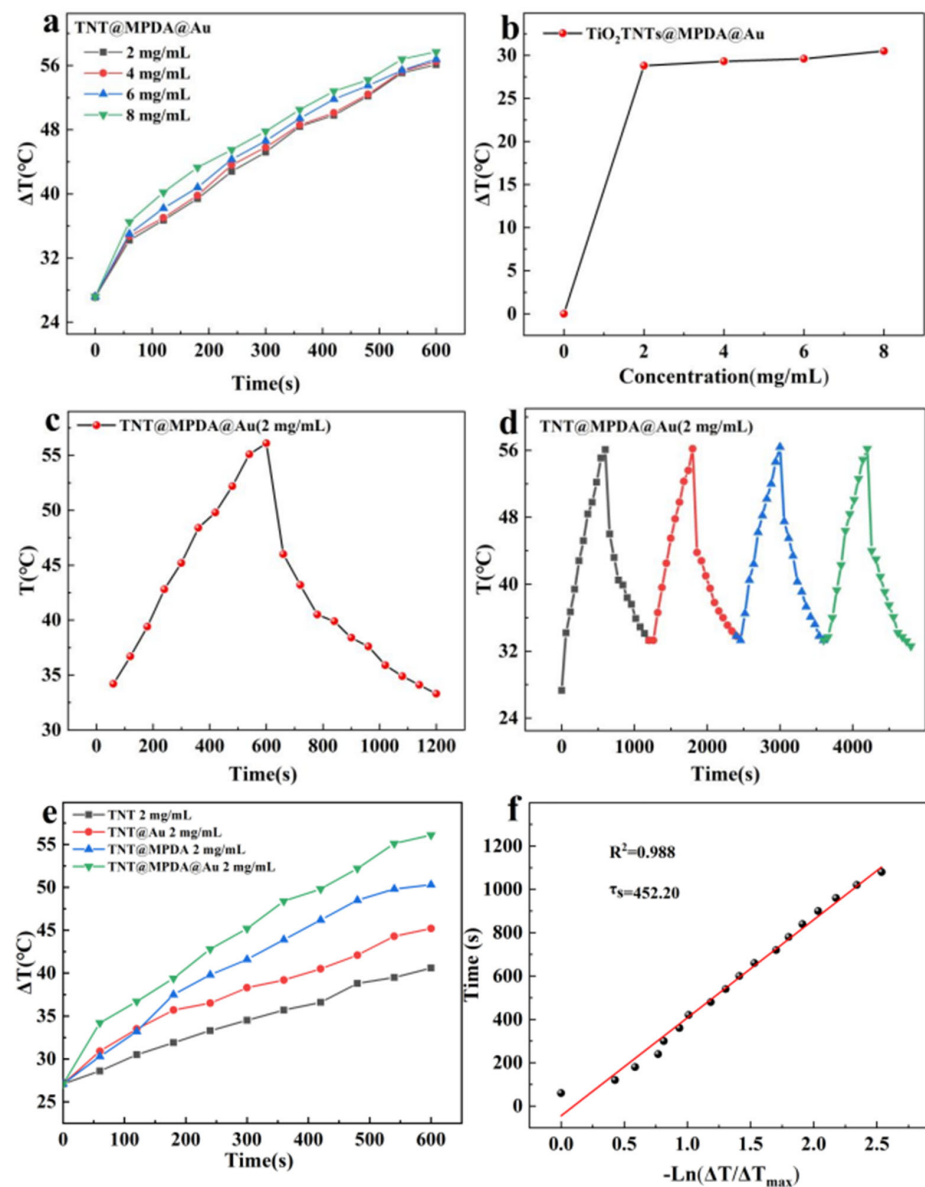


Figure 5. Temperature elevation of TNT@MPDA@Au nanotubes at various concentrations versus irradiation duration in 10 min (a). Temperature difference plots of TNT@MPDA@Au

nanotubes with different concentrations of TNT@MPDA@Au nanotubes after irradiation with near-infrared light for 10 min (b). Temperature rise and temperature drop curves of the 2 mg/mL of TNT@MPDA@Au nanotubes (c). Dispersion Temperature Change of 2 mg/mL TNT@MPDA@Au nanotubes during 4 Cycles (The black curve and square dots represent the first loop, the red curve and rounded dots represent the second loop, the blue curve and square triangle represent the third loop, and the green curve and inverted triangle represent the fourth loop.) of near-infrared irradiation (on/off) (d). Temperature changes of TNT, TNT@Au, TNT@MPDA, and TNT@MPDA@Au nanotubes after 10 min of NIR irradiation at a concentration of 2 mg/mL (e). The relationship between cooling time and temperature driving force of TNT@MPDA@Au nanotubes (f).

3.3. In Vitro Antibacterial Properties

The ideal wound dressing should have excellent antimicrobial properties to protect the wound from external bacteria. In order to investigate the antimicrobial properties of TNT@MPDA@Au nanotubes, a ring of inhibition experiments were carried out on *E. coli* and *S. aureus*, respectively. As shown in Figure 6a,c, the antimicrobial maps of the 2 bacteria after 24 h of exposure to natural light at 37 °C, respectively. From Figure 6a,c, it can be observed that both bacteria showed obvious inhibitory circles, indicating that the material has good antibacterial activity against both bacteria. Moreover, it could be observed from the difference in concentration gradients that the larger the concentration of the material, the larger the diameter of the inhibitory circle and the better the antimicrobial effect of the material. It was evident from the size of the circle of inhibition produced by the material against the two bacteria that the antimicrobial effect of the material was more prominent against *E. coli* as compared to *S. aureus*. This might be due to the fact that the peptidoglycan layer of *S. aureus* was usually much thicker than that of *E. coli*. Since PDA and AuNPs did not possess direct antimicrobial properties, the emergence of the inhibitory ring was attributed to TNTs [50,56].

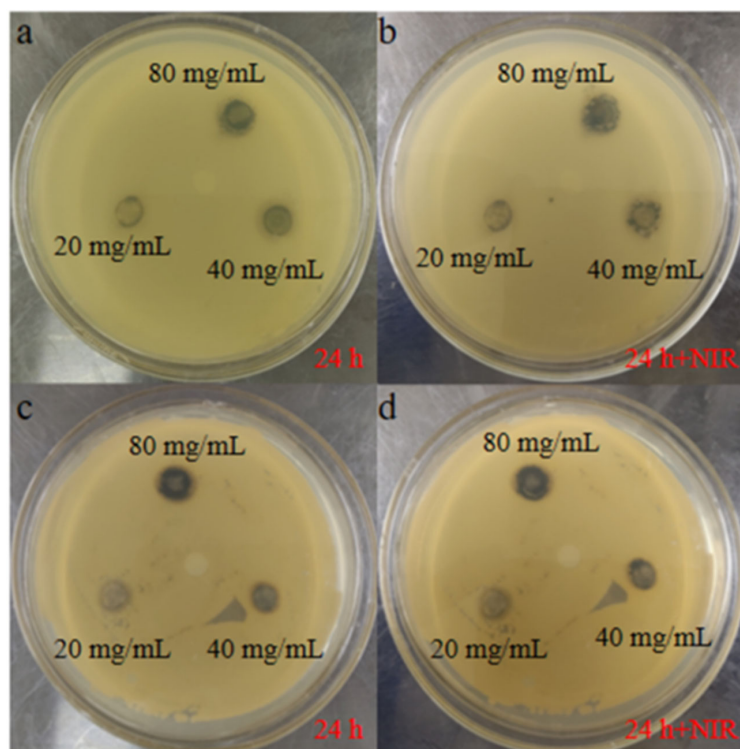


Figure 6. Antimicrobial effect of TNT@MPDA@Au nanotubes (20 mg/mL, 40 mg/mL, and 80 mg/mL) dropped into *E. coli* (a) and *S. aureus* (c) after 24 h of incubation, and photothermal antimicrobial effect on *E. coli* (b) and *S. aureus* (d) after 24 h, respectively.

Then, after 24 h of incubation, as shown in Figure 6b,d 2 bacteria grew again within the original inhibition circle, indicating that TNTs lack the ability to sustain antimicrobial activity over a long period of time. Therefore, secondary antimicrobials need to be carried out by a three-component synergistic photothermal method using TNT, MPDA, and Au. The photothermal test showed that TNT@MPDA@Au nanotubes had excellent photothermal performance, and the temperature could reach 57 °C at 8 mg/mL. As a result, under ten minutes of NIR, most of the bacteria in the inhibition circle underwent apoptosis, indicating that the nanotubes have excellent photothermal antibacterial properties [57]. Circle of inhibition sizes of *E. coli* and *S. aureus* were measured and the measured data are shown in Table 2.

Table 2. Circle of inhibition sizes of *E. coli* and *S. aureus*.

Concentration of TNT@MPDA@Au		0 mg/mL	20 mg/mL	40 mg/mL	80 mg/mL
Inhibitory Ring Size of Bacteria	<i>E. coli</i>	0 cm	0.22 cm	0.48 cm	0.6 cm
	<i>S. aureus</i>	0 cm	0.2 cm	0.36 cm	0.54 cm

3.4. In Vitro Cytotoxicity

Generally speaking, the toxicity and biocompatibility of antimicrobial materials are required to be high. The cytotoxicity of 293T normal cells was tested by the CCK8 method and the cell viability was determined. As shown in Figure 7, when the concentrations of TNT@MPDA nanotubes and TNT@MPDA@Au nanotubes were 200 µg/mL, the cell survival rates of normal cells, respectively, were 76.55% and 70.94%, indicating that the materials had good biocompatibility for normal cells. After NIR irradiation, the cell survival rate of TNT@MPDA nanotubes and TNT@MPDA@Au nanotubes against normal cells decreased to 75.03% and 66.36%, respectively. It could be clearly seen that the decrease in cell survival was not significant, indicating that the materials still had favourable biocompatibility after NIR. The above results demonstrated that normal cells were not greatly affected during in vivo and in vitro antimicrobial processes.

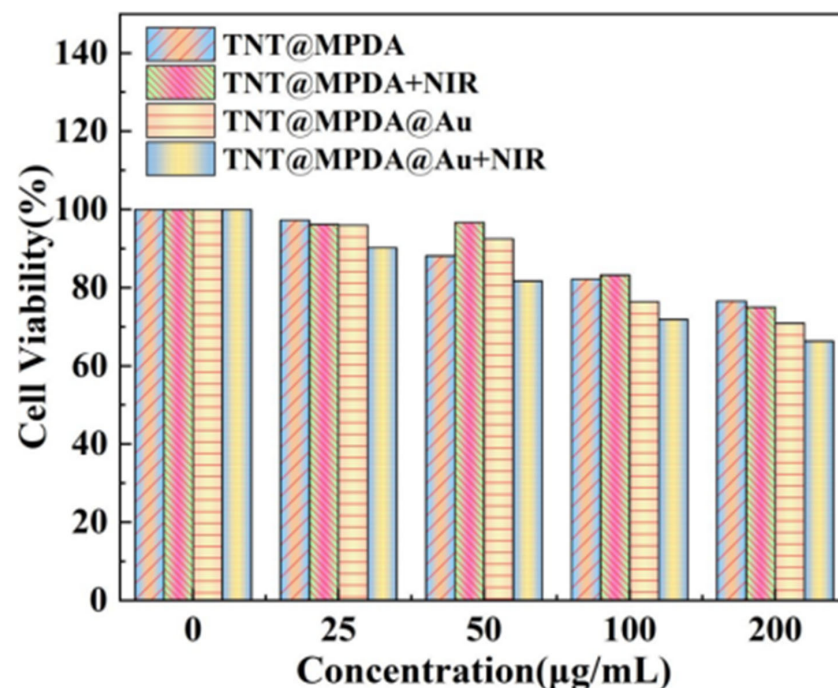


Figure 7. Cytotoxicity plots of TNT@MPDA nanotubes, TNT@MPDA nanotubes + NIR, TNT@MPDA@Au nanotubes + NIR, and TNT@MPDA@Au nanotubes incubated with 293T cells at 37 °C for 24 h.

3.5. Mechanical Properties of Hydrogels

In general, the wound-healing process was complex and there was an urgent need for multifunctional wound dressings. Adhesion of hydrogels has an excellent property of promoting wound closure and healing. Hydrogels adhere to tissues and can be used as an adhesive or sealant to avoid the loss of gas and fluid produced by the tissue. The adhesive properties of the hydrogel also allowed it to cope with a range of activities without being easily dislodged, thus increasing safety and prolonging the duration of use. Thus, an antimicrobial hybrid hydrogel possessing adhesion, injectability, self-healing, and plasticity was prepared to cope with cut wounds. The prepared multifunctional hybrid hydrogels not only could be directly antimicrobial and synergistically photothermal antimicrobial via TNTs but also the hydrogels themselves could promote wound healing. The adhesion properties of hydrogels of different concentrations were tested with the REVETEST scratch tester as shown in Figure 8a. The hydrogel films with different concentrations had better adhesion properties as the pressure exerted by the indenter and the depth of the scratches increased to withstand higher forces. Under the maximum force of 5 N, the forces at which the hydrogels of different concentrations were completely ruptured were $F_A = 2.02$ N, $F_B = 3.04$ N, and $F_C = 4.88$ N. The results show that the higher the concentration of hydrogel, the higher the force it can withstand and the better the adhesion performance. As shown in Figure 8b,c, both hydrogels could be written with clear letters on blank paper by 1 mL and 10 mL syringes, indicating that both prepared hydrogels have excellent injectability. Next, the self-healing properties of the hydrogel were observed through a more intuitive approach. The state of both hydrogels ranged from intact to cut in half to intact, indicating that both hydrogels have excellent self-healing properties. The remodelling properties of hydrogels allow for a wide range of wounds of different depths as well as different shapes. Both hydrogels could be easily changed in shape (rod; cube; and sphere), indicating that the prepared hydrogels have excellent remodelling properties [19].

Antimicrobial hydrogel with similar mechanical properties to the skin facilitates skin wound repair, maintains the integrity of the material, and facilitates good adhesion when the skin tissue is deformed by external forces. As shown in Figure 8d, these hydrogels exhibited excellent tensile properties (434.2% to 547.6%) and were far superior to the mechanical properties of human skin (60% to 75%). The elongation at break increased from 434.24% (0 wt%) to 444.7% (1.5 wt%) and 547.6% (3 wt%) when the TNT@MPDA@Au nanoparticles were added from 0 wt% to 3 wt%. To assess the mechanical properties of these hydrogels, compressive stress–strain measurements were also performed. As shown in Figure 8e, the stresses of pure PVA/PEG hydrogels and TNT@MPDA@Au@PVA/PEG hydrogels (3 wt%) were 505.7 KPa and 11.8 MPa, respectively, when the strain was 95%. The compressive stress of TNT@MPDA@Au@PVA/PEG hydrogels (3 wt%) was significantly much higher than that of the pure PVA/PEG hydrogel, suggesting that the prepared hybrid hydrogels had more excellent compressive properties. The enhancement of the tensile and compressive properties was due to the denser 3D network structure of PVA/PEG with the addition of TNT@MPDA@Au nanoparticles. As a result, these hydrogels with mechanical properties superior to those of human skin were able to resist external forces without breaking, avoiding damage to underlying tissues better [18].

The swelling degradation properties of hydrogels were one of the most essential properties of wound dressings. Adequate fluid absorption was required for bleeding control and exudate adsorption at the site of injury. And, appropriate swelling properties were also essential to keep the wound moist, which aids in the recovery of the wound surface. As shown in Figure 8f, the weight of these hydrogels increased rapidly during the initial phase, and the weight of these hydrogels increased by 437.1%, 404.9%, and 357.5% of the PBS solution, respectively, within 12 h. In addition, all of these hydrogels reached swelling equilibrium at 16 h. At equilibrium, these hydrogels absorbed 440.3%, 432.2%, and 364.6% by weight of PBS solution, respectively. The results showed that all of these hydrogels were rich in pores and could hold a large amount of water. The differences in the swelling ratios of the hydrogels were mainly due to the fact that the addition of TNT@MPDA@Au nanoparticles with different

masses made the pores of the pure PVA/PEG hydrogels smaller and led to the water not being easy to enter. Moreover, the decreasing swelling ratio with the increasing mass ratio of nanoparticles also indicated the formation of a more compact three-dimensional network structure. As shown in Figure 8g, all of these hydrogels were rapidly dehydrated within 3 h and the degradation rate reached about 100% at about 12 h, indicating that all the prepared hydrogels had excellent water retention properties [18,42].

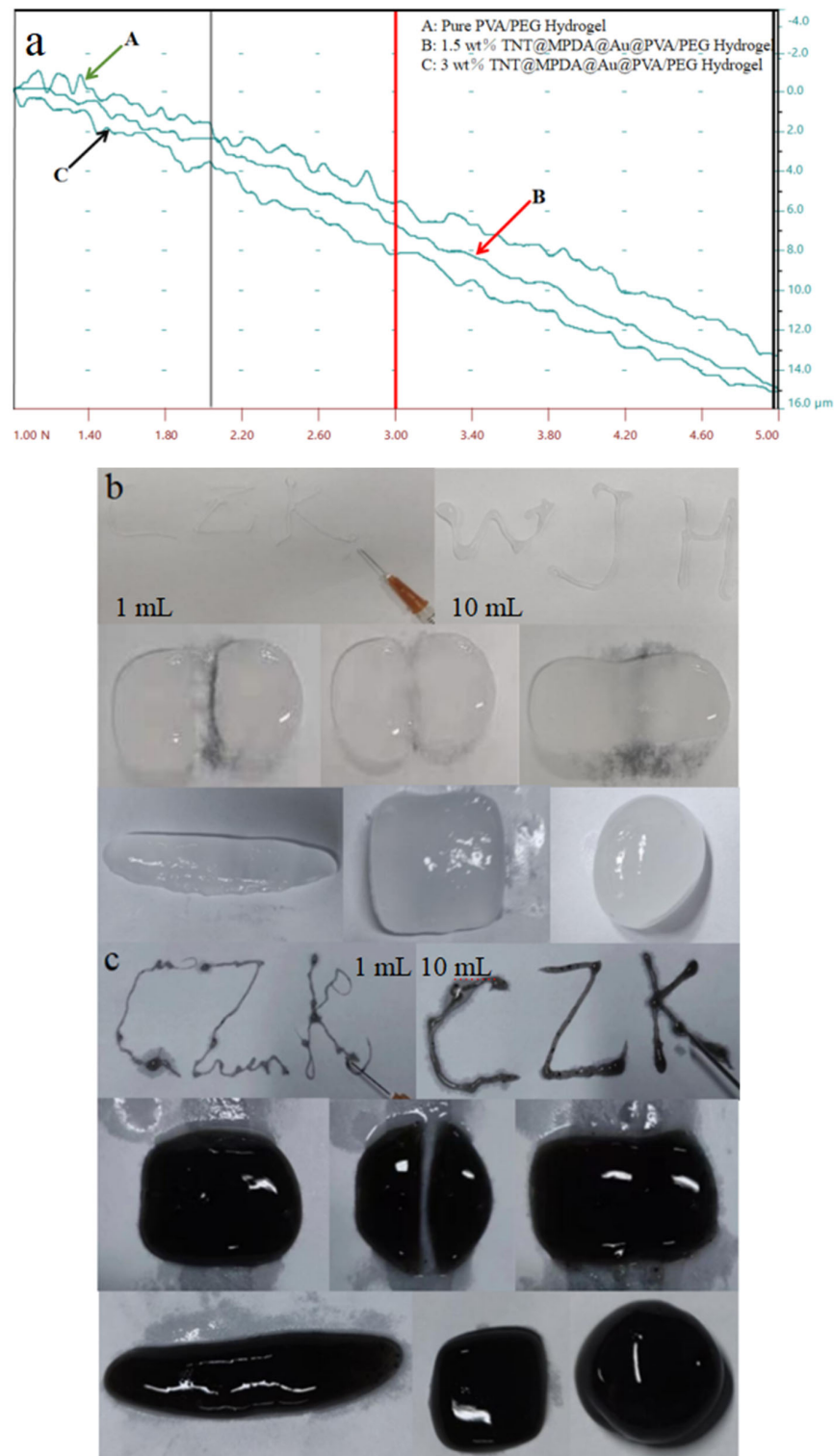


Figure 8. Cont.

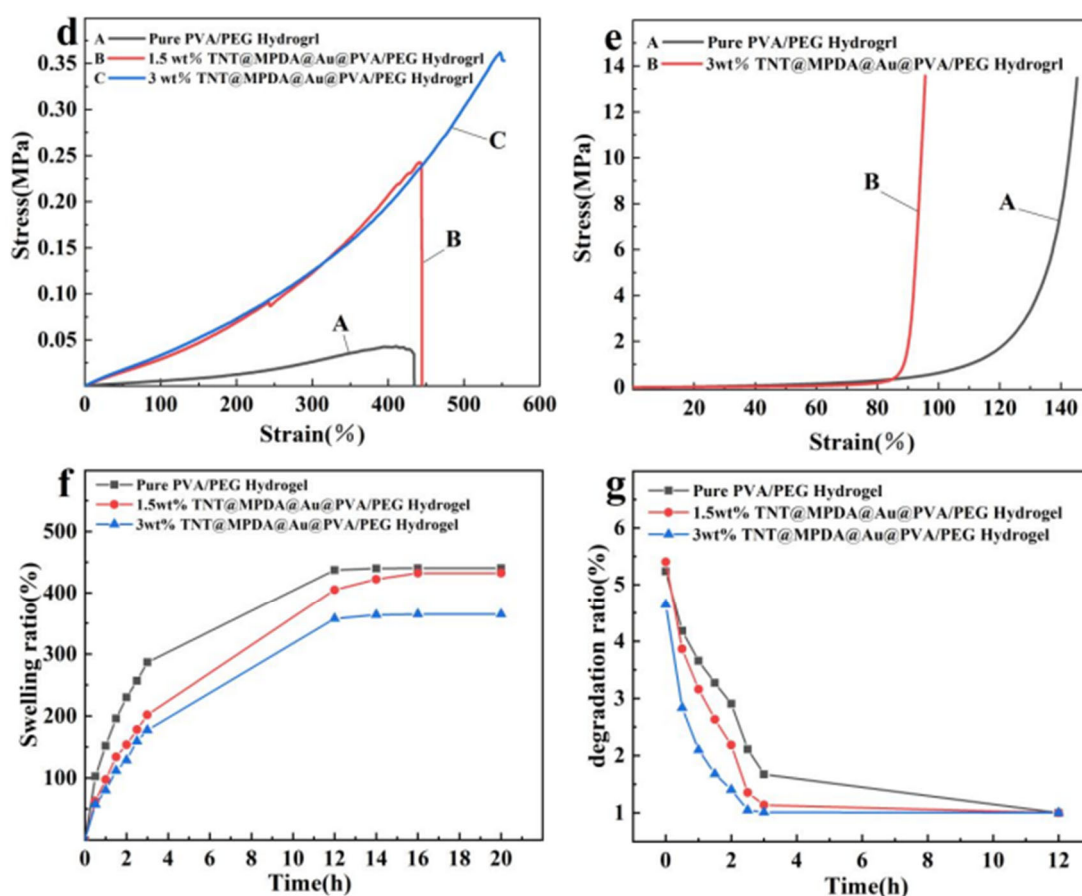


Figure 8. Adhesive properties of pure hydrogel and TNT@MPDA@Au@PVA/PEG hydrogel (a). Injectable, self-healing properties and remodelling of pure PVA/PEG hydrogel (b) and TNT@MPDA@Au@PVA/PEG hydrogel (c). Typical tensile stress-strain curves (d) and typical compression stress-strain curves (e), swelling curve (f) and degradation curve (g) for pure PVA/PEG hydrogel TNT@MPDA@Au@PVA/PEG hydrogels (1.5 wt%) and TNT@MPDA@Au@PVA/PEG hydrogels (3 wt%).

4. Conclusions

In summary, the TNT@MPDA@Au@PVA/PEG hydrogels prepared in this paper by a simple method have good biocompatibility and excellent photothermal antimicrobial and mechanical properties. In this paper, MPDA was used to improve the dispersion of AuNPs and increase the loading of AuNPs. Cytotoxicity experiments showed that the composite nanotubes had good biocompatibility. TNTs incorporated with AuNPs showed good antimicrobial properties under visible light photocatalysis, and even better antimicrobial ability after the addition of NIR. In mechanical property tests, the hydrogels showed good injectability, remodelling, self-healing, adhesion, water retention, water absorption, and tensile and compressive properties. This study is centred on a three-component photothermal antimicrobial with photocatalysis and good biocompatibility, which is important for improving the antimicrobial effect.

Author Contributions: Conceptualization, C.T.; Software, L.X.; Formal analysis, Q.Y.; Investigation, Z.C.; Resources, Z.C.; Data curation, Z.C., Q.Y. and W.G.; Writing—original draft, Z.C.; Writing—review & editing, C.T.; Project administration, C.T.; Funding acquisition, C.T. All authors have read and agreed to the published version of the manuscript.

Funding: This research was funded by Gansu Provincial Department of Education: Innovation Fund Project (2022A-043), the Basic Research Top Talent Training Program of Lanzhou Jiaotong University, and the Foundation of a Hundred Youth Talents Training Program of Lanzhou Jiaotong University.

Institutional Review Board Statement: Not applicable.

Informed Consent Statement: Not applicable.

Data Availability Statement: No new data were created or analyzed in this study.

Conflicts of Interest: The authors declare no conflict of interest.

References

1. Unnithan, A.R.; Nejad, A.G.; Sasikala, A.R.K.; Thomas, R.G.; Jeong, Y.Y.; Murugesan, P.; Nasser, S.; Wu, D.-M.; Park, C.H.; Kim, C.S. Electrospun zwitterionic nanofibers with in situ decelerated epithelialization property for non-adherent and easy removable wound dressing application. *Chem. Eng. J.* **2016**, *287*, 640–648. [[CrossRef](#)]
2. Luo, X.-G.; Zhang, H.; Cao, Z.-N.; Cai, N.; Xue, Y.-A.; Yu, F.-Q. A simple route to develop transparent doxorubicin-loaded nanodiamonds/cellulose nanocomposite membranes as potential wound dressings. *Carbohydr. Polym.* **2016**, *143*, 231–238. [[CrossRef](#)]
3. Xu, R.; Luo, G.-X.; Xia, H.-S.; He, W.-F.; Zhao, J.; Liu, B.; Tan, J.-L.; Zhou, J.-Y.; Liu, D.-S.; Wang, Y.-Z.; et al. Novel bilayer wound dressing composed of silicone rubber with particular micropores enhanced wound re-epithelialization and contraction. *Biomaterials* **2015**, *40*, 1–11. [[CrossRef](#)]
4. Zhao, X.; Liang, Y.; Huang, Y.; He, J.-H.; Han, Y.; Guo, B.-L. Physical double-network hydrogel adhesives with rapid shape adaptability, fast self-healing, antioxidant and NIR/pH stimulus-responsiveness for multidrug-resistant bacterial infection and removable wound dressing. *Adv. Funct. Mater.* **2020**, *30*, 1910748–1910765. [[CrossRef](#)]
5. Zhao, X.; Wu, H.; Guo, B.-L.; Dong, R.-N.; Qiu, Y.-S.; Peter, X.M. Antibacterial antioxidant electroactive injectable hydrogel as self-healing wound dressing with hemostasis and adhesiveness for cutaneous wound healing. *Biomaterials* **2017**, *122*, 34–47. [[CrossRef](#)] [[PubMed](#)]
6. Zhu, J.; Li, F.-X.; Wang, X.-L.; Yu, J.-Y.; Wu, D.-Q. Hyaluronic acid and polyethylene glycol hybrid hydrogel encapsulating nanogel with hemostasis and sustainable antibacterial property for wound healing. *ACS Appl. Mater. Interfaces* **2018**, *10*, 13304–13316. [[CrossRef](#)] [[PubMed](#)]
7. Wang, Y.; Yang, M.-R.; Zhao, Z. Facile fabrication of self-healing, injectable and antimicrobial cationic guar gum hydrogel dressings driven by hydrogen bonds. *Carbohydr. Polym.* **2023**, *310*, 120723–120732. [[CrossRef](#)] [[PubMed](#)]
8. Li, Y.-A.; Wang, J.-M.; Yang, Y.-Q.; Shi, J.; Zhang, H.-Y.; Yao, X.-H.; Chen, W.-Y.; Zhang, X.-Y. A rose bengal/graphene oxide/PVA hybrid hydrogel with enhanced mechanical properties and light-triggered antibacterial activity for wound treatment. *Mater. Sci. Eng. C* **2021**, *118*, 111447–111460. [[CrossRef](#)] [[PubMed](#)]
9. Song, S.; Liu, Z.; Abubaker, M.A.; Ding, L.; Zhang, J.; Yang, S.-R.; Fan, Z.-J. Antibacterial polyvinyl alcohol/bacterial cellulose/nano-silver hydrogels that effectively promote wound healing. *Mater. Sci. Eng. C* **2021**, *126*, 112171–112183. [[CrossRef](#)] [[PubMed](#)]
10. Chen, H.-L.; Cheng, J.-W.; Ran, L.-X.; Yu, K.; Lu, B.-T.; Lan, G.-Q.; Dai, F.-Y.; Lu, F. An injectable self-healing hydrogel with adhesive and antibacterial properties effectively promotes wound healing. *Carbohydr. Polym.* **2018**, *201*, 522–531. [[CrossRef](#)] [[PubMed](#)]
11. Renganathan, R.; Subha, V.; Sathya, R.; Ravindran, R.S.E. Silver nanoparticles from methanolic stem extract of *Gymnema sylvestre* and its characterisation studies. *Int. J. Nano Biomater.* **2017**, *7*, 1752–8933. [[CrossRef](#)]
12. Song, J.-W.; Yuan, C.-Q.; Jiao, T.-F.; Xing, R.-R.; Yang, M.-Y.; Adams, D.J.; Yan, X.-H. Multifunctional antimicrobial biometallohydrogels based on amino acid coordinated self-assembly. *Small* **2020**, *16*, 1907309–1907318. [[CrossRef](#)]
13. Tortorella, S.; Inzalaco, G.; Dapporto, F.; Maturi, M.; Sambri, L.; Vetri Buratti, V.; Chiariello, M.; Franchini, M.C.; Locatelli, E. Biocompatible pectin-based hybrid hydrogels for tissue engineering applications. *New J. Chem.* **2021**, *45*, 22386–22395. [[CrossRef](#)]
14. Gherardini, L.; Vetri Buratti, V.; Maturi, M.; Inzalaco, G.; Locatelli, E.; Sambri, L.; Gargiulo, S.; Barone, V.; Bonente, D.; Bertelli, E.; et al. Loco-regional treatment with temozolomide-loaded thermogels prevents glioblastoma recurrences in orthotopic human xenograft models. *Sci. Rep.* **2023**, *13*, 4630. [[CrossRef](#)]
15. Heiba, Z.K.; Mohamed, M.B.; Ahmed, S.I. Exploring the physical properties of PVA/PEG polymeric material upon doping with nano gadolinium oxide. *Alex. Eng. J.* **2022**, *61*, 3375–3383. [[CrossRef](#)]
16. Wang, Z.-H.; Ye, Q.-Z.; Yu, S.; Akhavan, B. Poly Ethylene Glycol (PEG)-based Hydrogels for Drug Delivery in Cancer Therapy: A Comprehensive Review. *Adv. Healthc. Mater.* **2023**, *12*, 2300105–2300150. [[CrossRef](#)] [[PubMed](#)]
17. Casettari, L.; Villasaliu, D.; Castagnino, E.; Stolnik, C.; Howdle, S.; Illum, L. PEGylated chitosan derivatives: Synthesis, characterizations and pharmaceutical applications. *Prog. Polym. Sci.* **2012**, *37*, 659–685. [[CrossRef](#)]
18. Fang, H.; Wang, J.-H.; Li, L.; Xu, L.-Q.; Wu, Y.-X.; Wang, Y.; Xu, F.; Tian, J.; Yao, L. A novel high-strength poly (ionic liquid)/PVA hydrogel dressing for antibacterial applications. *Chem. Eng. J.* **2019**, *365*, 153–164. [[CrossRef](#)]
19. Bo, Y.-Y.; Zhang, L.-H.; Wang, Z.-F.; Shen, J.-F.; Zhou, Z.-W.; Yang, Y.; Wang, Y.; Qin, J.-L.; He, Y.-N. Antibacterial Hydrogel with Self-Healing Property for Wound-Healing Applications. *ACS Biomater. Sci. Eng.* **2021**, *7*, 5135–5143. [[CrossRef](#)] [[PubMed](#)]
20. Wang, Z.-Y.; Yang, H.-T.; Liang, H.-B.; Xu, Y.-M.; Zhou, J.-P.; Peng, H.-X.; Zhong, J.; Xi, W.-X. Polydopamine particles reinforced poly(vinyl alcohol) hydrogel composites with fast self healing behavior. *Prog. Org. Coat.* **2020**, *143*, 105636–105644. [[CrossRef](#)]

21. Tao, C.-H.; Ma, F.-S.; Chen, T.-D.; Li, X.-Q.; Guan, W.-J.; Zhang, A.-Q. Facile synthesis and performance studies of BSA and PDA@Ag hollow microcapsules using SiO₂ microspheres as the templates. *J. Alloys Compd.* **2017**, *715*, 154–160. [[CrossRef](#)]
22. Zeng, J.-K.; Wang, Y.-T.; Suna, Z.-Y.; Chang, H.-H.; Cao, M.; Zhao, J.; Lin, K.; Xie, Y.-Z. A novel biocompatible PDA/IR820/DAP coating for antibiotic/photodynamic/photothermal triple therapy to inhibit and eliminate *Staphylococcus aureus* biofilm. *Chem. Eng. J.* **2020**, *394*, 125017–125029. [[CrossRef](#)]
23. Liu, J.-Y.; Liu, Y.-W.; Cao, Y.-D.; Sang, S.-H.; Guan, L.; Wang, Y.-Y.; Wang, J. Preparation of Fe₃O₄@PDA@Au@GO Composite as SERS Substrate and Its Application in the Enrichment and Detection for Phenanthrene. *Micromachines* **2022**, *13*, 128–141. [[CrossRef](#)] [[PubMed](#)]
24. Maturi, M.; Locatelli, E.; Sambri, L.; Tortorella, S.; Šturm, S.; Kostevšek, N.; Comes Franchini, M. Synthesis of ultrasmall single-crystal gold-silver alloy nanotriangles and their application in photothermal therapy. *Nanomaterials* **2021**, *11*, 912. [[CrossRef](#)]
25. Vines, J.B.; Yoon, J.H.; Ryu, N.E.; Lim, D.J.; Park, H. Gold nanoparticles for photothermal cancer therapy. *Front. Chem.* **2019**, *7*, 167. [[CrossRef](#)]
26. Li, H.-Y.; Lin, L.-L.; Su, S.-S.; Wen, X.-Y.; Yan, R.; Liu, H.-M.; Tao, C.-H. Enhanced photothermal effect of functionalized HMPDA@AuNPs microcapsules for near-infrared theranostic treatment of tumor. *J. Mater. Sci.* **2022**, *57*, 7694–7705. [[CrossRef](#)]
27. Jiang, K.; Smith, D.A.; Pinchuk, A. Size-dependent photothermal conversion efficiencies of plasmonically heated gold nanoparticles. *J. Phys. Chem. C* **2013**, *117*, 27073–27080. [[CrossRef](#)]
28. Cao, F.; Wei, C.; Ma, G.; Hou, L.; Zhang, R.; Mei, L.; Qin, Q. Synthesis of photothermal antimicrobial cotton gauze using AuNPs as photothermal transduction agents. *RSC Adv.* **2021**, *11*, 25976–25982. [[CrossRef](#)]
29. Liu, Y.-H.; Li, Z.-W.; Yin, Z.-B.; Zhang, H.-X.; Gao, Y.; Huo, G.-Y.; Wu, A.-J.; Zeng, L.-Y. Amplified photoacoustic signal and enhanced photothermal conversion of poly-dopamine-coated gold nanobipyramids for phototheranostics and synergistic chemotherapy. *ACS Appl. Mater. Interfaces* **2020**, *12*, 14866–14875. [[CrossRef](#)]
30. Wang, W.-J.; Liu, J.-L.; Feng, W.-J.; Du, S.-L.; Ge, R.; Li, J.; Liu, Y.; Sun, H.-C.; Zhang, D.-Q.; Zhang, H.; et al. Targeting mitochondria with Au-Ag@Polydopamine nanoparticles for papillary thyroid cancer therapy. *Biomater. Sci.* **2019**, *7*, 1052–1063. [[CrossRef](#)]
31. Moongraksathuma, B.; Chen, Y.-W. Anatase TiO₂ co-doped with silver and ceria for antibacterial application. *Catal. Today* **2018**, *310*, 68–74. [[CrossRef](#)]
32. Daghrir, R.; Drogui, P.; Robert, D. Modified TiO₂ for environmental photocatalytic applications: A review. *Ind. Eng. Chem. Res.* **2013**, *52*, 3581–3599. [[CrossRef](#)]
33. Pichat, P. Are TiO₂ nanotubes worth using in photocatalytic purification of air and water? *Molecules* **2014**, *19*, 15075–15087. [[CrossRef](#)] [[PubMed](#)]
34. Roy, P.; Berger, S.; Schmuki, P. TiO₂ nanotubes: Synthesis and applications. *Angew. Chem. Int. Edit.* **2011**, *50*, 2904–2939. [[CrossRef](#)] [[PubMed](#)]
35. Paramasivam, I.; Jha, H.; Liu, N.; Schmuki, P. A review of photocatalysis using self-organized TiO₂ nanotubes and other ordered oxide nanostructures. *Small* **2012**, *8*, 3073–3103. [[CrossRef](#)] [[PubMed](#)]
36. Xu, W.; Qi, M.; Li, X.; Liu, X.; Wang, L.; Yu, W.; Liu, M.; Lan, A.; Zhou, Y.; Song, Y. TiO₂ nanotubes modified with Au nanoparticles for visible-light enhanced antibacterial and anti-inflammatory capabilities. *Electroanal. Chem.* **2019**, *842*, 66–73. [[CrossRef](#)]
37. Camposeco, R.; Castillo, S.; Mejia-Centeno, I.; Navarrete, J.; Gómez, R. Effect of the Ti/Na molar ratio on the acidity and the structure of TiO₂ nanostructures: Nanotubes, nanofibers and nanowires. *Mater. Charact.* **2014**, *90*, 113–120. [[CrossRef](#)]
38. Chokesawatankit, N.; Jutakradsada, P.; Boonlue, S.; Knijnenburg, J.; Wright, P.; Sillanpää, M.; Kamwilaisak, K. Ag-doped Cobweb-like structure of TiO₂ nanotubes for antibacterial activity against Methicillin-resistant *Staphylococcus aureus* (MRSA). *J. Environ. Chem. Eng.* **2021**, *9*, 105843–105853. [[CrossRef](#)]
39. Seo, H.K.; Kim, G.S.; Ansari, S.G.; Kim, Y.S.; Shin, H.S.; Shim, K.H.; Suh, E.K. A study on the structure/phase transformation of titanate nanotubes synthesized at various hydrothermal temperatures. *Sol. Energy Mater. Sol. Cells* **2008**, *92*, 1533–1539. [[CrossRef](#)]
40. Lin, L.-L.; Li, H.-Y.; Su, S.-S.; Wen, X.-Y.; Yan, R.; Tao, C.-H. Study on the structure and properties of Fe₃O₄@HMPDA@HA magnetic hollow mesoporous submicron drug-carrying system. *Micropor. Mesopor. Mater.* **2022**, *330*, 111582–111592. [[CrossRef](#)]
41. Tao, C.-H.; Chen, T.-D.; Liu, H.; Su, S.-S. Design of biocompatible Fe₃O₄@MPDA mesoporous core-shell nanospheres for drug delivery. *Micropor. Mesopor. Mater.* **2020**, *293*, 109823–109842. [[CrossRef](#)]
42. Yan, P.-F.; Li, M.-Y.; Liu, J.; Hu, Y.-D.; Tang, K.Y. MoS₂@PDA@Ag/PVA Hybrid Hydrogel with Excellent Light-Responsive Antibacterial Activity and Enhanced Mechanical Properties for Wound Dressing. *Macromol. Mater. Eng.* **2021**, *307*, 2100654–2100666. [[CrossRef](#)]
43. Golabdar, A.; Adelnia, H.; Moshtzan, N.; Gavvani, J.N.; Izadi-Vasafi, H. Anti-bacterial poly(vinyl alcohol) nanocomposite hydrogels reinforced with in situ synthesized silver nanoparticles. *Polym. Compos.* **2019**, *404*, 1322–1328. [[CrossRef](#)]
44. Falqi, F.H.; Bin-Dahman, O.A.; Hussain, M.; Al-Harhi, M.A. Preparation of Miscible PVA/PEG Blends and Effect of Graphene Concentration on Thermal, Crystallization, Morphological, and Mechanical Properties of PVA/PEG (10wt%) Blend. *Int. J. Polym. Sci.* **2018**, *10*, 8527693–8527703. [[CrossRef](#)]
45. Wang, X.-X.; Cao, D.-W.; Tang, X.-J.; Yang, J.-J.; Jiang, D.-Y.; Liu, M.; He, N.-Y.; Wang, Z.-F. Coating Carbon Nanosphere with Patchy Gold for Production of Highly Efficient Photothermal Agent. *ACS Appl. Mater. Interfaces* **2016**, *8*, 19321–19332. [[CrossRef](#)]
46. Su, S.-S.; Lin, L.-L.; Li, H.-Y.; Wen, X.-Y.; Yan, R.; Tao, C.-H. Preparation and properties study of F-SiO₂@MPDA-AuNPs drug nanocarriers. *Micropor. Mesopor. Mater.* **2022**, *330*, 111571–111581. [[CrossRef](#)]

47. Roper, D.K.; Ahn, W.; Hoepfner, M. Microscale heat transfer transduced by surface plasmon resonant gold nanoparticles. *J. Phys. Chem. C* **2007**, *111*, 3636–3641. [[CrossRef](#)]
48. Tao, B.-L.; Lin, C.-C.; Yuan, Z.; He, Y.; Chen, M.-W.; Li, K.; Hu, J.-W.; Yang, Y.-L.; Xia, Z.-Z.-L.; Cai, K.-Y. Near infrared light-triggered on-demand currelease from Gel-PDA@Cur composite hydrogel for antibacterial wound healing. *Chem. Eng. J.* **2020**, *403*, 126182–126240. [[CrossRef](#)]
49. Li, L.-L.; Lin, L.-L.; Yan, R.; Chen, Z.-K.; Wen, X.-Y.; Zeng, X.-W.; Tao, C.-H. Multi-functional Fe₃O₄@HMPDA@G5-Au core-releasable satellite nano drug carriers for multimodal treatment of tumor cells. *Eur. Pol. J.* **2022**, *181*, 111647–111659. [[CrossRef](#)]
50. Shumbula, N.P.; Nkabinde, S.S.; Ndala, Z.B.; Mpelane, S.; Shumbula, M.P.; Mdluli, P.S.; Njengele-Tetyana, Z.; Tetyana, P.; Hlatshwayo, P.; Mlambo, M.; et al. Evaluating the antimicrobial activity and cytotoxicity of polydopamine capped silver and silver/polydopamine core-shell nanocomposites. *Arab. J. Chem.* **2022**, *15*, 103798–103810. [[CrossRef](#)]
51. Zeng, Q.-K.; Qian, Y.-N.; Huang, Y.-J.; Ding, F.; Qi, X.-L.; Shen, J.-L. Polydopamine nanoparticle-dotted food gum hydrogel with excellent antibacterial activity and rapid shape adaptability for accelerated bacteria-infected wound healing. *Bioact. Mater.* **2021**, *6*, 2647–2657. [[CrossRef](#)] [[PubMed](#)]
52. Cui, K.-X.; Yan, B.; Xie, Y.-J.; Qian, H.; Wang, X.-G.; Huang, Q.-X.; He, Y.-H.; Jin, S.-M.; Zeng, H.-B. Regenerable urchin-like Fe₃O₄@PDA-Ag hollow microspheres as catalyst and adsorbent for enhanced removal of organic dyes. *J. Hazard. Mater.* **2018**, *350*, 66–75. [[CrossRef](#)] [[PubMed](#)]
53. Tao, C.-H.; Chen, T.-D.; Liu, H.; Su, S.-S. Preparation and adsorption performance research of large-volume hollow mesoporous polydopamine microcapsules. *MRS Commun.* **2019**, *9*, 744–749. [[CrossRef](#)]
54. Vargas, M.A.; Rodríguez-Páez, J.E. Amorphous TiO₂ nanoparticles: Synthesis and antibacterial capacity. *J. Non-Cryst. Solids* **2017**, *459*, 192–205. [[CrossRef](#)]
55. Feng, X.-Y.; Wang, P.-F.; Hou, J.; Qian, J.; Wang, C.; Ao, Y.-H. Oxygen vacancies and phosphorus codoped black titania coated Carbon nano-tube composite photocatalyst with efficient photocatalytic performance for the degradation of acetaminophen under visible light irradiation. *Chem. Eng. J.* **2018**, *352*, 947–956. [[CrossRef](#)]
56. Arab, M.; Jallab, M.; Ghaffari, M.; Moghbelli, E.; Saeb, M.R. Synthesis, rheological characterization, and antibacterial activity of polyvinyl alcohol (PVA)/zinc oxide nanoparticles wound dressing, achieved under electron beam irradiation. *Iran. Polym. J.* **2021**, *30*, 1019–1028. [[CrossRef](#)]
57. Wang, H.-F.; Wei, L.-Y.; Wang, Z.-Q.; Chen, S.-G. Preparation, characterization and long-term antibacterial activity of Ag-poly(dopamine)-TiO₂ nanotubes composites. *Rsc. Adv.* **2016**, *6*, 14097–14104. [[CrossRef](#)]

Disclaimer/Publisher’s Note: The statements, opinions and data contained in all publications are solely those of the individual author(s) and contributor(s) and not of MDPI and/or the editor(s). MDPI and/or the editor(s) disclaim responsibility for any injury to people or property resulting from any ideas, methods, instructions or products referred to in the content.